An angular reduced order model for radiative transfer in non grey media

Laurent Soucasse[a,*], Andrew G. Buchan[b], Steven Dargaville[c], Christopher C. Pain[c]

[a] *Laboratoire EM2C, CNRS, CentraleSupélec, Université Paris-Saclay, 91192 Gif-sur-Yvette, France*
[b] *School of Engineering and Material Sciences, Queen Mary University of London, E1 4NS, United Kingdom*
[c] *Applied Modelling and Computation Group, Department of Earth Science and Engineering, Imperial College London, SW7 2AZ, United Kingdom*

Abstract

This paper investigates a reduced order model for the angular discretisation of the radiative transfer equation (RTE) when considering non grey participating gases. The key idea is to use a global model for the gas radiative properties and to derive an angular reduced order model, based on the Proper Orthogonal Decomposition (POD) method, for each absorption coefficient class independently. Angular POD basis functions are extracted from high order S_N reference solutions. A finite element approach is used to discretised the RTE in space and angle and the POD angular matrices of the reduced system are easily constructed from the S_N angular matrices of the reference solutions. The angular POD basis sets are truncated at different levels depending on the absorption coefficient class in order to optimally compute the total radiative power. The method is applied to solve the radia-

*Corresponding author.
Email address: laurent.soucasse@centralesupelec.fr (Laurent Soucasse)

tion field associated to an air/H_2O mixture flowing in a square differentially heated cavity, with black isothermal walls and diffuse reflecting adiabatic walls. Results show that the POD model is very accurate and efficient for treating the thick classes but it suffers from a low convergence rate for the thin classes. For computing the radiative power, the reduced order model allows to reduce the averaged number of angular basis functions of an order of magnitude and to reduce the CPU time by a factor 2 to 3 to reach a given level of accuracy, compared to a standard S_N method.
Keywords: reduced order model, angular discretisation, finite element, non grey media

1. Introduction

Despite today's large computational resources, the numerical simulation of radiative transfer remains a computational challenge owing to the high dimension of the phase-space (time, space, propagation direction and wavenumber) in which the radiative intensity varies. Many heat-transfer problems of interest involve for instance gaseous participating medium, whose absorption spectra are made of millions of lines, that flows in turbulent regime and covers a wide range of time and spatial scales. In the recent years, a wide literature has thus been devoted to reducing the computational requirements of radiation calculations while maintaining a high accuracy.

A simple strategy consists in adapting the discretisation by focusing the numerical effort in specific regions of the phase space where the gradients of the radiative intensity are localised and thus reducing the number of degrees of freedom of the discretised problem. This approach is generally not satis-

factory for the wavenumber dimension because of the line structure of the spectra and one has to employ proven methods such as correlated-k models, Statistical Narrow Band models or global models [1] to reduce the spectral complexity. However, substantial computational gains can be obtained by adapting the spatial or the angular resolution. Adaptive Mesh Refinement (AMR) techniques based on a hierarchy of structured meshes, have been used for instance by Ogando and Velarde [2] to optimise the radiation spatial discretisation while keeping a uniform discrete ordinates expansion for the angular dependence. Another spatial adaptivity algorithm has been developed by Yang and Yuan [3] for application to radiation transport coupled with Lagrangian hydrodynamics. Recently, an angular adaptivity method has been proposed by Soucasse *et al.* based on a hierarchical wavelet basis set whose expansion can be easily varied through the spatial domain without interpolation. This algorithm was associated to a goal-based error measure to accurately compute the radiative power.

Other approaches for decreasing computational requirements of radiative transfer calculations rely on multi-scale splitting. Roger *et al.* [4] and Coelho *et al.* [5] developed a hybrid transport-diffusion model well suited for radiative transfer close to the optically thick regime. They split the intensity into a macroscopic part calculated by a diffusion equation and a mesoscopic part calculated by a Monte Carlo or a discrete ordinates method. Soucasse *et al.* [6] proposed a sub-grid scale model dedicated to turbulent participating medium where large scale contributions are being solved by a reference ray tracing method and subgrid scale contributions are being solved by an approximate model in Fourier space.

In this article, we will focus on reduced order modelling for radiation transport. Reduced Order Models (ROM) are widely used in computational physics for decreasing the number of degrees of freedom of complex dynamical systems. They aim at finding a low order optimal basis able to represent a physical phenomenon or to condensate the response of a physical model to a set of parameters [7]. Most of ROMs rely on the Proper Orthogonal Decomposition (POD) method, although other modal decompositions are employed such as Dynamic Mode Decomposition [8], Proper Generalized Decomposition [9] or Branch Eigenmodes Reduction Method [10]. The POD is based on a statistical analysis of high-fidelity numerical data or experimental data. This method extracts from the data a few dominant uncorrelated modes, that are able to capture the underlying physics without any a priori knowledge of it. However, the prediction capabilities of POD-based ROMs are often restricted to a small variation of input parameters around the conditions under which the data were obtained. In addition, their computational efficiency are affected by the computational cost of the full order model when POD relies on numerical data. POD has been widely used in fluid mechanics, where spatial basis functions are extracted from high resolution spatial fields (snapshots) recorded through time [11, 12], to model turbulent pipe flow [13], natural convection [14] or pollutant transport in street canyons [15].

In the field of radiative transfer, such model reduction techniques have been applied by Pinnau and Schultze [16] for treating the spectral dependence of the radiative intensity. They used a POD method to model the radiative properties of glass and compared their approach to the Weighted-Sum-of-Grey-Gas (WSGG) method and a simple frequency averaging. Buchan *et*

al. [17] were the first to propose a POD reduced order model for resolving the angular dimension of the Boltzmann transport equation. Angular POD basis functions were derived from high order spherical harmonics expansion solutions and applied to solve neutron transport problems. Tencer *et al.* [18, 19] followed a similar approach to build optimal angular basis functions from high order discrete ordinates expansions. They developed a greedy algorithm for improving the snapshot sampling, that selects angular regions with the highest angular residual. They applied their model to one- and three-dimensional test problems but only considered grey absorbing medium without any scattering or reflection by the walls.

The angular dependence of the radiative field is known to vary a lot with the optical thickness, between the thin kinetic regime and the thick diffuse regime. The goal of this paper is to investigate the suitability of an angular ROM for thermal radiation calculations involving actual participating gases and thus covering a large optical thickness range. The key idea is to use a global model for the gas radiative properties and to derive an angular ROM from high order discrete ordinates expansions, based on the POD method, for each absorption coefficient class independently. The method is applied to solve the radiation field associated to an air/H_2O mixture flowing in a square differentially heated cavity, with black isothermal walls and diffuse reflecting adiabatic walls. The angular POD basis sets are truncated at different levels depending on the absorption coefficient class in order to optimally compute the total radiative power. The sections of this article are set out as follows. The numerical methods and models used for discretising the radiative transfer equation are detailed in Sec. 2 and the angular ROM is presented in Sec. 3.

The accuracy and efficiency of the angular ROM for computing the incident radiation of each absorption class and for computing the total radiative power is finally assessed in Sec. 4.

2. Radiative tranfer equation and numerical modelling

For a non-scattering medium of optical index equal to 1 at local thermal equilibrium, the Radiative Transfer Equation (RTE) is given by

$$\boldsymbol{\Omega} \cdot \boldsymbol{\nabla} I_\nu(\boldsymbol{r}, \boldsymbol{\Omega}) = \kappa_\nu(\boldsymbol{r}) \left(I_{b\nu}(T(\boldsymbol{r})) - I_\nu(\boldsymbol{r}, \boldsymbol{\Omega}) \right), \tag{1}$$

where $I_\nu(\boldsymbol{r}, \boldsymbol{\Omega})$ is the radiative intensity at wavenumber ν, point $\boldsymbol{r}$ and direction $\boldsymbol{\Omega}$, $I_{b\nu}(T(\boldsymbol{r}))$ is the blackbody intensity at local temperature $T(\boldsymbol{r})$ and $\kappa_\nu(\boldsymbol{r})$ is the spectral absorption coefficient of the medium.

In physical domains bounded by grey opaque walls, diffusely reflecting, the associated boundary condition writes

$$I_\nu(\boldsymbol{r}_w) = \varepsilon(\boldsymbol{r}_w) I_{b\nu}(T(\boldsymbol{r}_w)) + \frac{1 - \varepsilon(\boldsymbol{r}_w)}{\pi} \int_{\boldsymbol{\Omega}' \cdot \boldsymbol{n} < 0} I_\nu(\boldsymbol{r}_w, \boldsymbol{\Omega}') |\boldsymbol{\Omega}' \cdot \boldsymbol{n}| d\boldsymbol{\Omega}', \tag{2}$$

for points $\boldsymbol{r}_w$ and directions $\boldsymbol{\Omega}$, such that $\boldsymbol{\Omega} \cdot \boldsymbol{n} > 0$, $\boldsymbol{n}$ being the wall normal directed towards the inside of the domain and $\varepsilon(\boldsymbol{r}_w)$ being the wall emissivity.

The radiative power $\mathcal{P}^{rad}(\boldsymbol{r})$ in the medium is defined as the difference between the absorbed radiative power and the emitted radiative power and is equal to the opposite of the divergence of the radiative flux $\boldsymbol{q}^{rad}(\boldsymbol{r})$

$$\mathcal{P}^{rad}(\boldsymbol{r}) = -\boldsymbol{\nabla} \cdot \boldsymbol{q}^{rad}(\boldsymbol{r}) = \int_\nu \kappa_\nu(\boldsymbol{r}) \left(G_\nu(\boldsymbol{r}) - 4\pi I_{b\nu}(T(\boldsymbol{r})) \right) d\nu, \tag{3}$$

where $G_\nu(\boldsymbol{r})$ is the incident radiation given by

$$G_\nu(\boldsymbol{r}) = \int_{\boldsymbol{\Omega}} I_\nu(\boldsymbol{r}, \boldsymbol{\Omega}) d\boldsymbol{\Omega}. \tag{4}$$

This power takes part in the energy balance of the material system and this is the quantity we want to accurately compute in coupled heat transfer problems.

2.1. Radiative property modelling

The spectral dependence of the absorption coefficient κ_ν is taken into account using a global model based on absorption distribution functions [20]. In the practical problem addressed in Section 4, the absorption coefficient is assumed to be homogeneous and is computed at a reference temperature T_{ref}. In that case, the absorption distribution function writes

$$\mathcal{F}(k) = \frac{\pi}{\sigma T_{\text{ref}}^4} \int_{\nu,\, \kappa_\nu(T_{\text{ref}}) \leq k} I_{b\,\nu}(T_{\text{ref}}) d\nu. \tag{5}$$

This distribution is a function of the values of the absorption coefficient k and is discretised in intervals $[k_i^-; k_i^+]$ of averaged value k_i. The weights of this distribution associated with each interval i are defined as $w_i = \mathcal{F}(k_i^+) - \mathcal{F}(k_i^-)$. Equations (1) and (2) then become

$$\boldsymbol{\Omega} \cdot \boldsymbol{\nabla} I_i(\boldsymbol{r}, \boldsymbol{\Omega}) = k_i \left(\frac{w_i \sigma T^4(\boldsymbol{r})}{\pi} - I_i(\boldsymbol{r}, \boldsymbol{\Omega}) \right), \tag{6}$$

$$I_i(\boldsymbol{r}_w) = \varepsilon(\boldsymbol{r}_w) \frac{w_i \sigma T^4(\boldsymbol{r}_w)}{\pi} + \frac{1 - \varepsilon(\boldsymbol{r}_w)}{\pi} \int_{\boldsymbol{\Omega}' \cdot \boldsymbol{n} < 0} I_i(\boldsymbol{r}_w, \boldsymbol{\Omega}') |\boldsymbol{\Omega}' \cdot \boldsymbol{n}| d\boldsymbol{\Omega}', \tag{7}$$

where σ is the Stefan-Boltzmann constant. The radiative intensity integrated over the wavenumber is simply retrieved by summing the contributions of each k-class: $I = \int I_\nu d\nu = \sum_i I_i$.

This global model is advantageous because the integration over the wavenumber is replaced by an integration over the absorption coefficient k, for which a coarse discretisation is sufficient. Another benefit is that it will be possible

to associate with each k-class a different angular discretization, adapted to the corresponding optical thickness range.

As a homogeneous medium is considered, the model error only lies in the discretisation in k. In the case of a heterogeneous media, the global model can also be applied providing additional assumptions. In that case one can define a unique k-discretisation with weights depending on the local properties of the medium (temperature, pressure, composition), see for instance Refs. [21–23]. The numerical methods and the angular reduced order model presented in this paper can thus be easily extended to the case of heterogeneous media.

The global model is however restricted to gray wall emissivities and gray scattering. Gray scattering is not considered in this work but its addition would be straightforward and would not affect the angular reduction method [17].

2.2. Angular discretisation

The angular general expansion is achieved by a finite element method. The angular dependence of the radiative intensity associated with the k-class of index i, is restricted to the function space spanned by a set of $\mathcal{M}_i$ angular basis functions $\{\mathcal{G}_{iq}(\mathbf{\Omega})\}$ for $q \in \{1, 2, \cdots, \mathcal{M}_i\}$

$$I_i(\mathbf{\Omega}, \boldsymbol{r}) \simeq \sum_{q=1}^{\mathcal{M}_i} \mathcal{G}_{iq}(\mathbf{\Omega}) \mathcal{I}_{iq}(\boldsymbol{r}), \tag{8}$$

$\mathcal{I}_{iq}(\boldsymbol{r})$ being the coefficients of the projection onto the basis. It should be noted that the set of angular basis functions as well as the size of the basis can be different for each k-class of index i.

Introducing the expansion (8) into Eq. (6) and applying Galerkin projection leads to the following angular linear system in Cartesian coordinates

$$\mathsf{A}_{i,x}\frac{\partial \boldsymbol{\mathcal{I}}_i(\boldsymbol{r})}{\partial x} + \mathsf{A}_{i,y}\frac{\partial \boldsymbol{\mathcal{I}}_i(\boldsymbol{r})}{\partial y} + \mathsf{A}_{i,z}\frac{\partial \boldsymbol{\mathcal{I}}_i(\boldsymbol{r})}{\partial z} + \mathsf{H}_i\boldsymbol{\mathcal{I}}_i(\boldsymbol{r}) = \boldsymbol{\mathcal{S}}_i(\boldsymbol{r}) \tag{9}$$

where $\boldsymbol{\mathcal{I}}_i(\boldsymbol{r})$ is a vector of size $\mathcal{M}_i$ containing the projection coefficients $\mathcal{I}_{iq}(\boldsymbol{r})$. $\mathsf{A}_{i,\,x/y/z}$ and H_i are the angular matrices defined by

$$(\mathsf{A}_{i,\,x/y/z})_{p,q} = \int \Omega_{x/y/z}\mathcal{G}_{ip}(\boldsymbol{\Omega})\mathcal{G}_{iq}(\boldsymbol{\Omega})d\boldsymbol{\Omega}, \tag{10}$$

$$(\mathsf{H}_i)_{p,q} = k_i \int \mathcal{G}_{ip}(\boldsymbol{\Omega})\mathcal{G}_{iq}(\boldsymbol{\Omega})d\boldsymbol{\Omega}, \tag{11}$$

and $\boldsymbol{\mathcal{S}}_i(\boldsymbol{r})$ is the angular source term vector whose components are

$$\mathcal{S}_{iq}(\boldsymbol{r}) = k_i w_i \frac{\sigma T^4(\boldsymbol{r})}{\pi} \int \mathcal{G}_{iq}(\boldsymbol{\Omega})d\boldsymbol{\Omega}. \tag{12}$$

This general framework holds for various angular discretisations such as discrete ordinates, spherical harmonics, wavelets, and it also suits for the angular reduced order model (see Section 3). In the following we will use the discrete ordinates method (S_N) as the reference method for angular discretisation. A finite element formulation of the method is implemented here which is not strictly equivalent to the standard quadrature-based S_N method. It consists in dividing the angular domain into $\mathcal{M} = N\times(N+2)$ nonoverlapping solid angles $\Delta\Omega_p$ of equal size and defining $\mathcal{M}$ piece-wise constant angular basis functions associated to each angular interval such that $\mathcal{G}_p(\boldsymbol{\Omega}) = 1$ if $\boldsymbol{\Omega} \in \Delta\Omega_p$ and 0 otherwise. Without scattering, it should be noted that the angular matrices associated to the discrete ordinates discretisation are diagonal.

2.3. Spatial discretisation

A variational multiscale finite element method [24] is used to perform the spatial discretisation. This approach combines a continuous finite element representation with a discontinuous subgrid scale (SGS) model. The spatial variations of the angular coefficients $\boldsymbol{\mathcal{I}}_i(\boldsymbol{r})$ are decomposed into a coarse component $\overline{\boldsymbol{\mathcal{I}}}_i(\boldsymbol{r})$ and a subgrid component $\widetilde{\boldsymbol{\mathcal{I}}}_i(\boldsymbol{r})$. The coarse component is assumed to lie in a continuous finite element space, spanned by η_N basis functions, while the subgrid component is assumed to lie in a discontinuous space, spanned by η_Q basis functions, such that

$$\boldsymbol{\mathcal{I}}_i(\boldsymbol{r}) \simeq \sum_{j=1}^{\eta_N} N_j(\boldsymbol{r}) \overline{\boldsymbol{\mathcal{I}}}_{ij} + \sum_{j=1}^{\eta_Q} Q_j(\boldsymbol{r}) \widetilde{\boldsymbol{\mathcal{I}}}_{ij}. \tag{13}$$

The continuous basis functions $N_j(\boldsymbol{r})$ and the discontinuous basis functions $Q_j(\boldsymbol{r})$ are associated with the same spatial mesh and are both piecewise linear across the spatial elements in this work. The same spatial mesh is used for each k-class.

Using decomposition of Eq. (13) into Eq. (9) and applying Galerkin projection in space leads to a space-angle block linear system of size $\mathcal{M}_i \times (\eta_N + \eta_Q)$ that has to be solved for each k-class i. The role of the subgrid component is to suppress any instability and non-physical oscillations that may arise from a continuous finite element discretisation of the RTE. However, the method enables the subgrid scale component of the solution to be eliminated from the resulting system of discretised equations so that a single linear system of size $\mathcal{M}_i \times \eta_N$ is solved. The main advantage of the method is to provide accurate and numerically stable solutions, similar to those obtained from a discontinuous Galerkin formulation, but with much lower number of

spatial degrees of freedom. More details on the implementation, the accuracy and the efficiency of the subgrid scale model can be found in Ref. [24].

Boundary conditions are implemented using a Riemann decomposition method in order to separate the incoming and outgoing part of the radiative flux at the boundaries. This is a general technique that applies to any type of angular discretisation (S_N, P_N, wavelets...) including the POD angular discretisation [25].

2.4. Implementation and validation

The space-angle linear system is solved using the generalised minimal residual method (GMRES) with a successive over-relaxation (SOR) preconditioner. We use the PETSc library [26] for the solver implementation. The same algorithms are used for solving the space-angle linear system resulting from the angular reduced order model.

The results of the present code have been successfully compared with reference results obtained with the Monte Carlo method on the 3D benchmark case of Ref. [27]. Relative differences were of the order of the standard deviation of the Monte Carlo calculation and were about 10^{-3}. The details and the results of this comparison have been already published in a previous study [28].

3. Reduced order model for the angular discretisation

The Proper Orthogonal Decomposition (POD) method applied to the angular discretisation of the RTE aims at constructing an optimal angular basis for a given problem based on a set of data representative of the angular variations of the radiative intensity. The method extracts from the data a

hierarchical basis set that can be truncated to any size depending on the desired accuracy.

3.1. Building the POD angular basis functions

The method of snapshots is used here to build the POD angular basis functions. The method is applied independently to each k-class in order to form adapted POD basis functions to each optical thickness range. An accurate solution of the problem of interest is generated using a reference model for the angular discretisation. We use here a high order discrete ordinates method S_N, with the same number of angular degrees of freedom $\mathcal{M}$ for each k-class. The reference angular coefficients at each spatial node $j = 1, \cdots, \eta$ are stored in column to form the following snapshot matrix S_i of size $\mathcal{M} \times \eta_N$ for each k-class i

$$S_i = [\boldsymbol{\mathcal{I}}_{i1}, \cdots, \boldsymbol{\mathcal{I}}_{ij}, \cdots, \boldsymbol{\mathcal{I}}_{i\eta_N}]. \tag{14}$$

Note that compared to standard POD methods, snapshots are recorded through space instead of time: the role of space and time dimensions are swaped with angle and space dimensions respectively.

The POD method consists in searching for the eigenvalue decomposition of the symmetric matrix $S_i S_i^T$

$$S_i S_i^T = U_i \Lambda_i U_i^T, \tag{15}$$

where Λ_i is a diagonal matrix containing the eigenvalues of the decomposition, that are all positive and ranked in decreasing order. The matrix U_i contains the eigenvectors of the decomposition: it represents a change-of-basis matrix between the S_N angular basis functions and the POD angular basis functions. Therefore, the POD angular basis functions $\{\mathcal{G}_{iq}^P(\boldsymbol{\Omega})\}, q \in$

$\{1, 2, \cdots, \mathcal{M}\}$ are obtained by combining the POD eigenvectors (the columns of the matrix U_i) with the S_N angular basis functions $\{\mathcal{G}_q(\mathbf{\Omega})\}, q \in \{1, 2, \cdots \mathcal{M}\}$, such that

$$\mathcal{G}_{iq}^P(\mathbf{\Omega}) = \sum_{p=1}^{\mathcal{M}} (U_i)_{p,q} \mathcal{G}_p(\mathbf{\Omega}). \tag{16}$$

Instead of building separated angular POD basis functions for each k-class, we could have built combined angular POD basis functions based on a single snapshot matrix that gathers all the angular coefficients at each spatial points for all the k-classes. Such reduction approach is however inefficient in terms of accuracy and computational time for the practical case addressed in Sec. 4 because it cannot correctly capture the angular behaviour of both the optically thin and optically thick regimes. A separated approach in energy for angular reduction was also shown to be much more efficient than a combined approach for neutron transport [29].

3.2. Building the angular reduced order model

The POD basis functions form a hierarchical basis set that can be truncated to any size. The aim of the reduced order model is to restrict this basis set to the first $\mathcal{M}_i^P$ basis functions ($\mathcal{M}_i^P < \mathcal{M}$) with the highest eigenvalues, which means they are the best for reconstructing the snapshot matrix in terms of the Frobenius norm.

In the reduced order model, we will assume that the angular variations of the radiative intensity associated to the k-class i can be captured using a few numbers of POD angular basis functions $\mathcal{M}_i^P$

$$I_i(\mathbf{\Omega}, \boldsymbol{r}) \simeq \sum_{q=1}^{\mathcal{M}_i^P} \mathcal{G}_{iq}^P(\mathbf{\Omega}) \mathcal{I}_{iq}^P(\boldsymbol{r}), \tag{17}$$

where $\mathcal{I}_{iq}^{P}(\boldsymbol{r})$ are the angular coefficients in the POD space. These POD angular coefficients are linked with those of the reference model using

$$\boldsymbol{\mathcal{I}}_i(\boldsymbol{r}) = U_i \, \boldsymbol{\mathcal{I}}_i^P(\boldsymbol{r}). \tag{18}$$

Note that only the first $\mathcal{M}_i^P$ columns of the matrix U_i are kept here, such that U_i is of size $\mathcal{M} \times \mathcal{M}_i^P$.

The efficiency of the truncation for representing accurately the reference calculation will depend on the decay of the eigenvalue spectrum: the faster is the decay, the lower is the number of POD basis functions necessary. Using Eq. (17), the discretised angular system of Eq. (9) can be formally rewritten as

$$\mathsf{A}_{i,x}^P \frac{\partial \boldsymbol{\mathcal{I}}_i^P(\boldsymbol{r})}{\partial x} + \mathsf{A}_{i,y}^P \frac{\partial \boldsymbol{\mathcal{I}}_i^P(\boldsymbol{r})}{\partial y} + \mathsf{A}_{i,z}^P \frac{\partial \boldsymbol{\mathcal{I}}_i^P(\boldsymbol{r})}{\partial z} + \mathsf{H}_i^P \boldsymbol{\mathcal{I}}_i^P(\boldsymbol{r}) = \boldsymbol{\mathcal{S}}_i^P(\boldsymbol{r}), \tag{19}$$

where $\mathsf{A}_{i,x/y/z}^P$ and H_i^P are the POD angular matrices of size $\mathcal{M}_i^P \times \mathcal{M}_i^P$ and $\boldsymbol{\mathcal{S}}_i^P(\boldsymbol{r})$ is the POD angular source vector of size $\mathcal{M}_i^P$. However, the POD angular matrices and the POD angular source vector can be easily formed from the reference model angular matrices $\mathsf{A}_{i,x/y/z}$ and H_i of size $\mathcal{M} \times \mathcal{M}$ and angular source vector $\boldsymbol{\mathcal{S}}_i(\boldsymbol{r})$ of size $\mathcal{M}$ in the full S_N space, using the change-of-basis matrix U_i (see Eq. (16)). Eq. (19) becomes then

$$U_i^T \mathsf{A}_{i,x} U_i \frac{\partial \boldsymbol{\mathcal{I}}_i^P(\boldsymbol{r})}{\partial x} + U_i^T \mathsf{A}_{i,y} U_i \frac{\partial \boldsymbol{\mathcal{I}}_i^P(\boldsymbol{r})}{\partial y} + U_i^T \mathsf{A}_{i,z} U_i \frac{\partial \boldsymbol{\mathcal{I}}_i^P(\boldsymbol{r})}{\partial z} + U_i^T \mathsf{H}_i U_i \boldsymbol{\mathcal{I}}_i^P(\boldsymbol{r}) = U_i^T \boldsymbol{\mathcal{S}}_i(\boldsymbol{r}). \tag{20}$$

This means the angular ROM can be easily implemented from the forward discretised angular system. Further details on the implementation of the angular ROM can be found in Ref. [17].

It should be emphasized here that a unique POD angular basis set is formed per k-class by condensing the reference angular information throughout the spatial domain. Thus, the POD angular expansion does not change with the spatial position. In addition, the size of the POD truncation $\mathcal{M}_i^P$ is kept constant across space, although it can be varied with the k-class i.

4. Results

In order to assess the suitability of an angular POD model for radiative heat transfer calculations in non grey media, we consider the natural convection of an actual radiating gas in a square differentially heated cavity. The cavity is made of two black vertical walls maintained at fixed temperature T_h and T_c and two adiabatic, perfectly diffuse reflecting walls. It is filled with humid air at a mean temperature $T_0 = 294.2$ K and at atmospheric pressure (Prandtl number of Pr $= 0.709$). We fix the cavity size to $L = 1$ m and we choose a moderate value of the Rayleigh number of $\mathrm{Ra} = g\beta(T_h - T_c)L^3/(\nu a) = 5 \times 10^6$ in order to obtain a steady natural convection flow. This gives a small temperature difference $T_h - T_c$ of about 5×10^{-2} K.

The finite element fluid dynamics code Fluidity [30] is used to solve the mass, momentum and energy balance under Boussinesq approximation without radiative energy source term. A $\mathbb{P}_1^{\mathrm{CG}}$ discretisation is applied for pressure, temperature and velocity fields together with an unstructured spatial grid made of about 4400 elements. We have checked mesh independence by doubling the number of elements and the difference in the total Nusselt number at the isothermal walls does not exceed 2 %. A Crank-Nicolson time

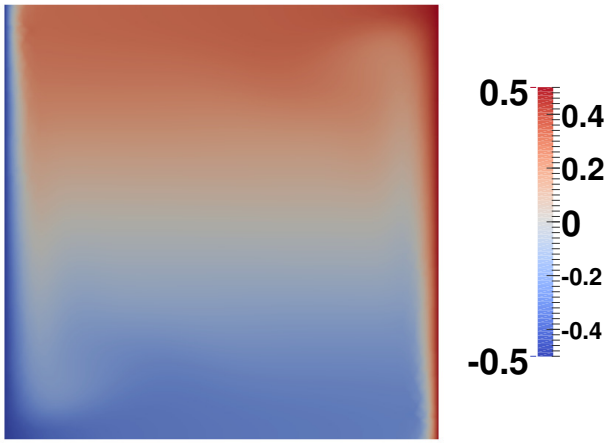

Figure 1: Snapshot of the reduced temperature field $(T - T_0)/(T_h - T_c)$ considered in the radiation calculations.

integration scheme is implemented to converge towards the steady solution. The resulting steady temperature field is shown in Fig. 1. It displays typical patterns of natural convection flows in differentially heated cavities such as the vertical boundary layers along the isothermal walls and the thermally stratified core.

The global model for the radiative properties of the participating mixture is built from the Line-By-Line (LBL) spectrum of the absorption coefficient at the reference temperature T_0 and with a molar fraction of water vapour of 2 %. This high resolution spectrum has been computed with the HITRAN 2008 database [31] with a resolution of 0.025 cm^{-1} and the corresponding absorption distribution function has been calculated from Eq. 5 at T_0. The values of the absorption coefficient go from $k_{\mathrm{min}} = 1.36 \times 10^{-6}$ m^{-1} to $k_{\mathrm{max}} =$

5.83×10^2 m^{-1}. We consider a transparent class from $k_{\min}$ to $k_{\text{cut}} = 10^{-3}$ m^{-1} and we logarithmically discretize the range $[k_{\text{cut}}; k_{\max}]$ into $N_k = 9$ classes. The emission of the transparent class is taken into account for computing the radiative source term. The accuracy of the model compared to the LBL approach is examined from emissivity calculation of isothermal columns of different lengths at T_0. Relative errors between LBL results and global model results do not exceed 1 %.

The angular POD reduction is performed from a reference radiation calculation using the temperature snapshot of Fig. 1 and a S_{26} discrete ordinates method (364 angular basis functions) for the angular discretisation of each of the nine k-classes. The process detailed in Sec. 3 is applied to build the angular POD basis functions and derive the angular reduced order model. The accuracy and efficiency of the model in solving the reference problem is then compared to the discrete ordinates method. In Sec. 4.1 we will focus on the computation of the incident radiation field $G_i(\boldsymbol{r})$ of each k-class i and in Sec. 4.2 we will focus on the computation of the radiative power $\mathcal{P}^{rad}(\boldsymbol{r})$.

4.1. Computing the incident radiation for each k-class

In this section we will first examine the accuracy and efficiency of the POD model for computing the incident radiation for each k-class separately. Radiation calculations are carried out with the POD model for different levels of truncation of the POD expansion, and with the discrete ordinates method for different order N. For each calculation (POD or S_N) the following error measure for the incident radiation is computed

$$e_i = \frac{\int (G_i(\boldsymbol{r}) - G_i^{\text{ref}}(\boldsymbol{r}))^2 d\boldsymbol{r}}{\int (G_i^{\text{ref}}(\boldsymbol{r}) - G_{\text{b}i}(T(\boldsymbol{r})))^2 d\boldsymbol{r}}, \tag{21}$$

where the superscript "ref" refers to the reference S_{26} solution and $G_{\mathrm{b}i}(\boldsymbol{r}) = 4w_i\sigma T^4(\boldsymbol{r})$ corresponds to the blackbody emission.

This error measure is plotted against the angular basis size in Fig. 2 for four of the nine k-classes, associated with different optical thicknesses ($k_2L = 8.87 \times 10^{-3}$, $k_4L = 1.70 \times 10^{-1}$, $k_6L = 3.24$, $k_8L = 62.0$). It could be noted that the convergence of the S_N method is not much affected by the optical thickness: for each k-class, the error roughly scales in $\mathcal{M}^{-1}$, $\mathcal{M}$ being the angular basis size. However, for the POD model, the convergence strongly differs between thin and thick classes. For the thin classes (k_2 and k_4) the error first oscillates above the S_N curve but then strongly drops and the POD model becomes between 10 to 100 times more accurate than the S_N method for the same basis size. For the thick classes (k_6 and k_8) the error is always below the S_N one. The decay is smooth, faster than for the S_N method, and roughly scales as $\mathcal{M}^{-2}$. From about 20 basis functions, the POD model is between 10 to 100 times more accurate than the S_N method.

To further analyse the accuracy of the POD model, the spatial distribution of the difference with the reference solution is showed in Fig. 3 for the third and seventh classes ($k_2L = 8.87 \times 10^{-3}$, $k_7L = 14.2$) when using 60 basis functions for both POD and S_N. Is also showed in Fig. 3 the reference incident radiation. For the third (thin) class, wall to wall and wall to gas transfer are dominant. Radiative transfer is very directional and the difference distribution follows dominant propagation directions for both POD and S_N, although differences are lower in the POD model. This error structure is partly due to slight ray effects remaining in the reference solution. For the seventh (thick) class, wall to gas and gas to gas transfer are dominant

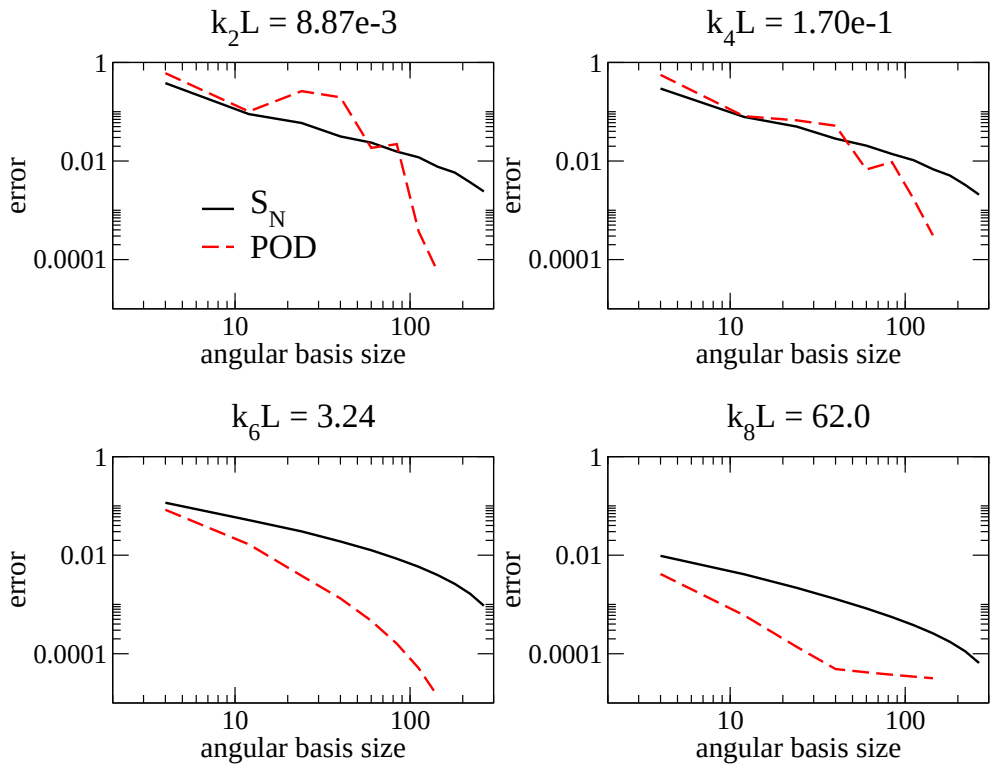

Figure 2: Incident radiation error norm (as defined in Eq. (21)) as a function of the angular basis size for four k-classes. Comparison between discrete ordinates (black plain lines) and POD models (red dashed lines).

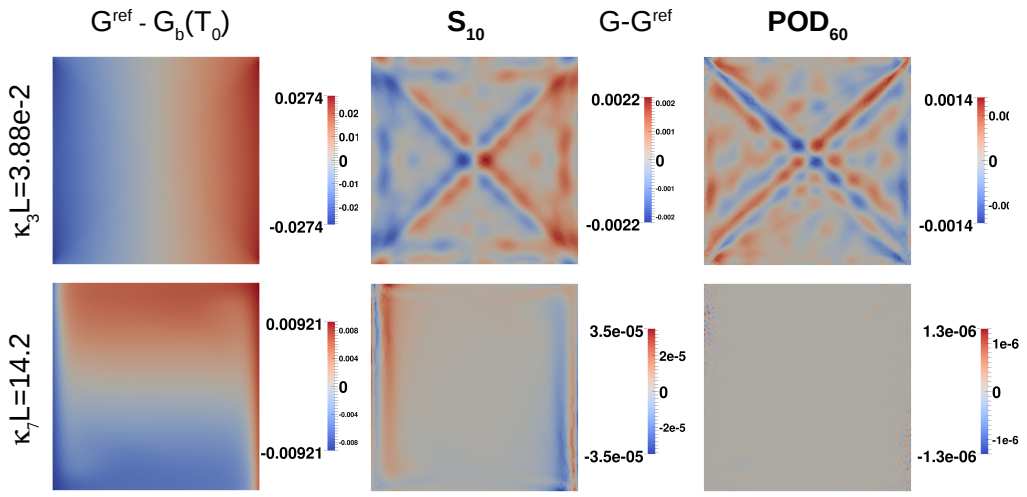

Figure 3: Reference incident radiation G^{ref} (left), difference with S_{10} calculation (middle) and difference with POD_{60} calculation (right), for the third k-class (top, $k_3 L = 3.88 \times 10^{-2}$) and for the seventh k-class (bottom, $k_7 L = 14.2$)

and the spatial distribution of the incident radiation follow the patterns of the temperature field. The differences in the S_N method are located along the isothermal walls where the incident radiation gradients are the strongest. Little differences can be also observed near the isothermal walls with the POD model but an order of magnitude lower than with the S_N method.

In order to understand the convergence properties of the POD model, the eigenvalue spectrum of the decomposition is presented in Fig. 4 for five of the nine k-classes. Larger eigenvalues are obtained for the thin classes because the weight w_i (see Eq. (6)) associated with the radiation emission of the k-class i decreases with the optical thickness. Each spectrum is characterized by a dominant first eigenvalue, representing the mean angular distribution but the decay of the next eigenvalues changes with the optical thickness. For

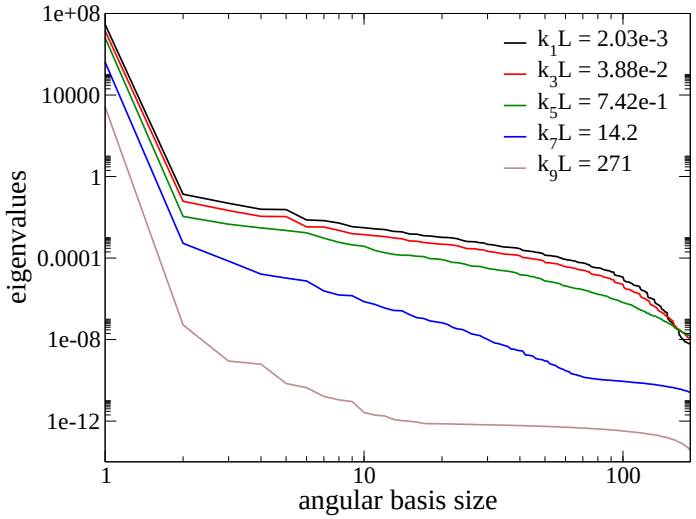

Figure 4: Eigenvalue spectrum of the POD for five k-classes.

the thin classes, the decay is slower meaning that the angular information is more difficult to condensate and that a large number of POD basis function is necessary to reconstruct the data. At the optically thin limit, the propagation directions are indeed strongly coupled because of the diffuse reflection of top and bottom walls. On the contrary, for the thick classes, the decay is faster meaning that the POD model is able to extract a few dominant eigenmodes. Comparing the convergence plots of Fig. 2 with the eigenspectra of Fig. 4 it can be noticed that the error decay with the number of POD basis functions scales with the square root of the eigenspectrum decay. This is a very interesting result that can be used to define a priori truncation level for the POD expansion to reach a given level of accuracy. This feature will be used in Sec. 4.2 to select the most appropriate POD basis size for each k-class.

The six first POD basis functions $\mathcal{G}^P(\mathbf{\Omega})$ are shown in Figs. 5 and 6 for the third and seventh k-classes, respectively. The basis functions are displayed in one projected hemisphere as the angular domain is restricted to polar angle $\theta \in [0; \pi/2]$ and azimuth angle $\phi \in [0; 2\pi]$ for a two-dimensional spatial domain. For the third (thin) class, the POD basis functions are characterized by sharp variations with the azimuthal angle, designed to capture the incident radiation from the walls from any spatial point of the medium. Additional variations are noticeable in the polar angle, due to the multiple reflections by the top and bottom diffuse walls that creates very large optical paths. The first POD mode displays a horizontal propagation direction corresponding to the mean energy transfer between the two isothermal black walls. For the seventh (thick) class, the POD basis functions have smoother shapes with respect to both polar and azimuthal angle. The first mode captures a mean diagonal propagation direction representative of radiative exchange between hot gas in the top right corner of the cavity and cold gas in the bottom left corner of the cavity.

So far, we have seen that the POD model is able to provide more accurate results than the S_N method for a given angular basis size, although the reduction is more efficient when increasing the optical thickness. We will now assess the computational efficiency of the reduced order model. The error measure of Eq. (21) is plotted against the CPU time in Fig. 7 for four of the nine k-classes (the same as in Fig. 2) for both POD and S_N. For the thin classes (k_2 and k_4), the POD model does not show any computational gain, except for the highest angular discretisation. However, for the thick classes (k_6 and k_8), a computational speed up to reach a given error level is observed

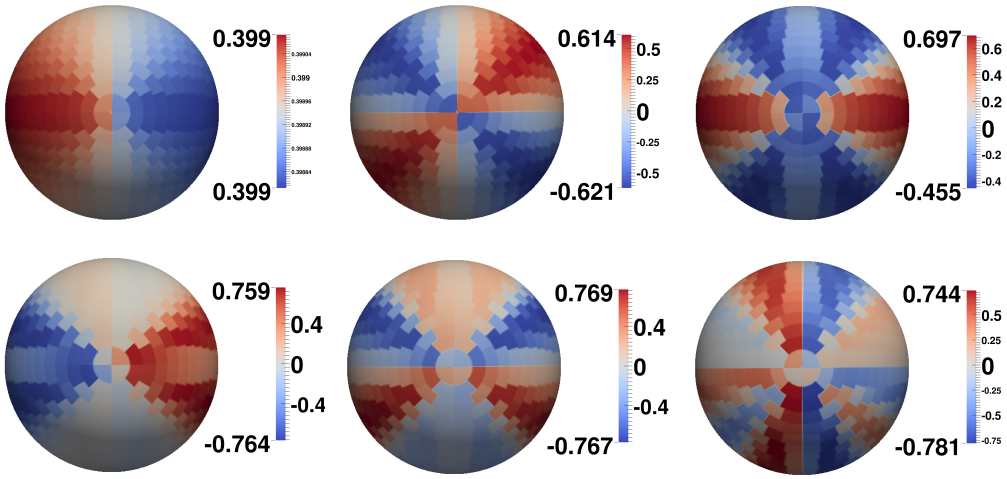

Figure 5: The first six POD basis functions, from left to right and from top to bottom, for the third k-class, $k_3 L = 3.88 \times 10^{-2}$.

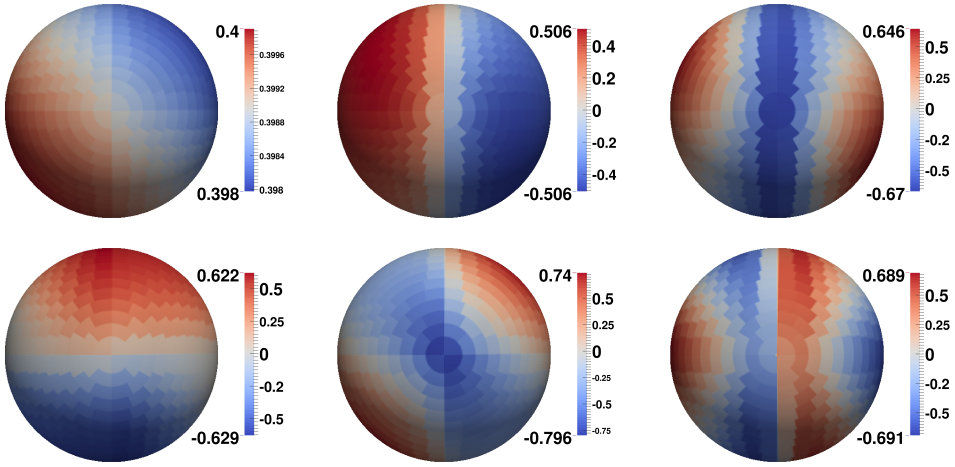

Figure 6: The first six POD basis functions, from left to right and from top to bottom, for the seventh k-class, $k_7 L = 14.2$.

and reaches an order of magnitude for a large range of angular basis size. For a given angular basis size, the POD model is actually more computationally expensive than the S_N method because the POD basis functions lead to the formation of dense angular matrices and it is more time consuming to assemble and solve the associated linear system. This additional computational cost varies with the optical thickness: POD is around 5 times slower than S_N for a thick class and around 10 times slower for a thin class. For the optically thin classes, the POD model suffers from a very low convergence rate of the linear solver. A very high number of iterations is necessary to converge suggesting that the linear system is ill-conditioned. However, the convergence is much faster for the thick classes: the number of solver iteration is 400 times larger (in average) for the first k-class ($k_1 L = 2.03 \times 10^{-3}$) compared to the last k-class ($k_9 L = 271$). This is further confirmed by an estimation of the condition number of the space-angle matrix that is of the order of 100 for the thin classes while it is of the order of unity for the thick classes. Finally, it should be noted that the computational time required for generating the snapshot data was not considered here, though it should be taken into account for assessing the efficiency of a predictive POD model. It is around 2×10^4 s in the present case.

4.2. Computing the radiative power

When studying natural convection of radiating gases, the objective is more to compute the radiative power rather than to compute the incident radiation for each k-class, because the radiative power is the coupling quantity that goes into the energy balance of the material system. We will thus assess in this section the efficiency of the POD model in computing the ra-

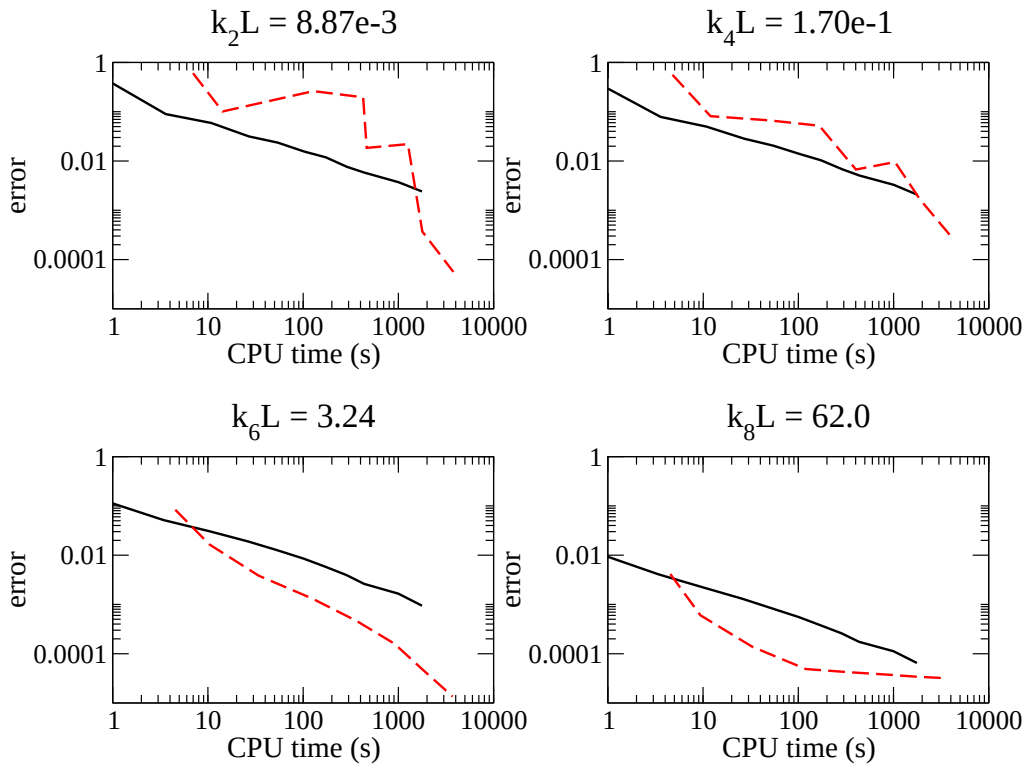

Figure 7: Incident radiation error norm (as defined in Eq. (21)) as a function of computational time for four k-classes. Comparison between discrete ordinates (black plain lines) and POD models (red dashed lines).

diative power given by

$$\mathcal{P}^{rad}(\boldsymbol{r}) = \sum_i k_i G_i(\boldsymbol{r}) - \sum_i w_i k_i 4\sigma T^4(\boldsymbol{r}). \tag{22}$$

The second emission term of Eq. (22) being deterministic, numerical errors only lie in the evaluation of the first absorption term, that is equal to the sum over all the k-classes of the incident radiation weighted by the absorption coefficient.

The results of Sec. 4.1 have shown that the number of POD basis function to reach a given error level on the incident radiation is not the same for each k-class and that this error scales with the square root of the eigenvalue spectrum of the POD. In order to find a priori the best POD basis size $\mathcal{M}_i^P$ for each k-class i for optimally computing the radiative power, we propose a simple error scaling based on the eigenvalue spectrum and the optical thickness. It consists in adding POD functions onto the angular basis until the following criteria is satisfied

$$\lambda_{i,m} k_i L < \tau^2, \tag{23}$$

where τ is a given tolerance and $\lambda_{i,m}$ is the m^{th} eigenvalue for k-class i, and fix the basis size $\mathcal{M}_i^P = m$. The resulting distribution of angular basis size across the optical thickness range is presented in Fig. 8 for different tolerance values. This distribution has a bell shape: the maximum angular resolution is put for the fourth and fifth classes. A low angular resolution is put in the thinnest classes because they do not contribute much to the radiative power, although the associated eigenspectrum decay is slow. On the contrary the thickest classes contribute a lot to the radiative power but the angular information is efficiently reduced by the POD, and again only

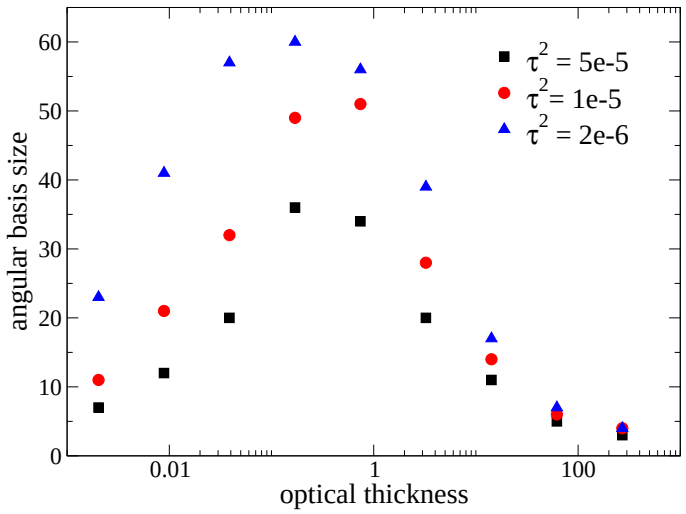

Figure 8: Distribution of angular basis size accross the optical thickness range in the optimised POD* model for different tolerance values τ.

a few POD basis functions are retained. This optimised POD discretisation will be noted POD* in the following.

We will now compare the accuracy and efficiency of uniform POD (same number of basis functions for each k-class), optimised POD* (using the basis function distribution of Fig. 8) and uniform discrete ordinates using the following error measure

$$e = \frac{\int (\mathcal{P}^{\mathrm{rad}}(\boldsymbol{r}) - \mathcal{P}^{\mathrm{rad,ref}}(\boldsymbol{r}))^2 d\boldsymbol{r}}{\int \mathcal{P}^{\mathrm{rad,ref}}(\boldsymbol{r})^2 d\boldsymbol{r}}, \tag{24}$$

where the superscript "ref" refers to the reference S_{26} solution. This error measure is given against the averaged angular basis size in Fig. 9 and against the computational time in Fig. 10 for POD, POD* and S_N models. For the optimised POD* model, the points in the graphs correspond to tolerance values in the range $\tau^2 \in [5 \times 10^{-5}; 2 \times 10^{-6}]$. Compared to the discrete

ordinates method, the uniform POD model has a faster convergence rate and uses less basis functions to reach a given error level but this angular reduction is not sufficient to obtain an actual gain in terms of computational time. However, the optimised POD* model allows for a much higher reduction of the averaged angular basis size leading to a significant time saving. Compared to the discrete ordinates method, the optimised POD* model uses about 10 times less angular basis functions and 2 to 3 times less computational time to reach a given error level. Interestingly, we have noticed the error e in the optimised POD* model roughly equals the tolerance τ of the heuristic scaling (23) used for the truncation of each class. This feature will be very useful for developping predictive POD models but need to be confirmed in other test problems.

5. Conclusion

This paper has presented a reduced order model for discretizing the angular dimension of the radiative transfer equation in non grey media. The POD method has been used to extract angular basis functions from high order discrete ordinates solutions. A finite element approach has been used to discretised the RTE in space and angle and the POD angular matrices of the reduced system has been easily constructed from the S_N angular matrices of the reference system. The method has been applied independently to each absorption coefficient class built from a global model of the radiative properties of the medium, allowing the angular basis functions to be tailored to a given optical thickness. The suitability of the POD model for thermal radiation has been assessed by computing the radiation field associated with

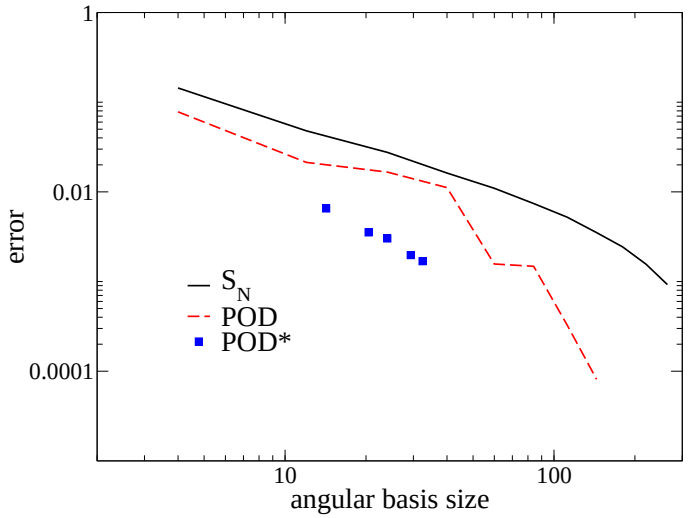

Figure 9: Radiative power error norm (as defined in Eq. (24)) as a function of the averaged angular basis size. Comparison between discrete ordinates (black plain lines), uniform POD (red dashed lines) and optimised POD* (blue squares) models.

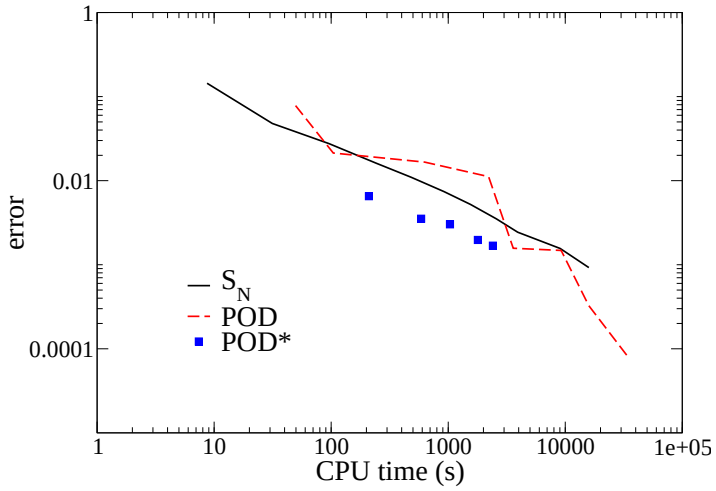

Figure 10: Radiative power error norm (as defined in Eq. (24)) as a function of computational time. Comparison between discrete ordinates (black plain lines), uniform POD (red dashed lines) and optimised POD* (blue squares) models.

a humid air flowing in a square differentially heated cavity.

Results have shown that the POD model is very accurate and efficient for treating the thick classes: for reaching the same accuracy on the incident radiation, the CPU time is reduced by an order of magnitude compared to the S_N method. However, the thin classes suffer from a low convergence rate probably due to the reflections by the boundaries in the problem considered. For computing the radiative power, we have proposed a simple scaling based on the POD eigenspectrum and the optical thickness, in order to find the optimal POD basis size for each absorption coefficient class. The computational effort is put on the intermediate optical thickness range as the optically thin classes do not contribute much to the radiative power and the angular behaviour of the optically thick classes is efficiently condensed by the POD. This optimised POD angular size distribution allows us to reduce the averaged number of angular basis function of an order of magnitude and to reduce the CPU time by a factor 2 to 3 to reach a given level of accuracy on the radiative power, compared to the S_N method. The heuristic scaling that gives this optimised angular distribution would need however to be tested in other problems.

This study focused on the ability of the angular POD model to reproduce the reference results. Future research will investigate the prediction capabilities of the POD model when changing the radiative properties of the medium or when considering time-dependent problems. Although the angular dependence of the radiation field varies a lot with the optical thickness between the thinnest class ($kL \sim 10^{-3}$) and the thickest class ($kL \sim 10^{3}$), it could be assumed that the angular POD basis are well adapted for an optical thickness

range (typically of the order of 5 to 10) and not only for a single value of the absorption coefficient. This would allow to predict the radiation field associated with another participating medium, with a different distribution of the global model parameters (k_i, w_i). This capability has been demonstrated in a recent work [29] on neutron transport in reactor physics where angular POD basis functions were built from snapshots computed with varying material cross-sections and the associated angular ROM was efficient in solving unseen problems with different properties. Moreover, when studying turbulent flows (higher Rayleigh number in the considered problem), the radiation computation needs to be repeated as the temperature field evolves. Because the angular POD basis functions do not seem to be strongly affected by the details of the temperature field, they could be potentially used for a large number of radiation calculations over time and thus provide a substantial computational gain in coupled flow/radiation problems.

Finally, other perspectives concern the improvement of the computational efficiency of this angular POD model. The solving time of the discretised linear system could be decreased by developing dedicated preconditioner, especially for optically thin media. The gappy POD technique [32] could also be used to coarsen the spatial resolution of the reduced order model. A last strategy for further decreasing the angular number of degrees of freedom (and thus improve the efficiency) would be to vary the POD basis size through the spatial domain. Such angular adaptivity algorithm would be possible because of the hierarchical nature of the POD basis functions.

Acknowledgments Andrew Buchan acknowledges funding through the

EPSRC grant EP/M022684/2. Steven Dargaville acknowledges support from the EPSRC through the funding of the EPSRC grant EP/P013198/1.

References

[1] J. Taine, A. Soufiani, Gas IR radiative properties: from spectroscopic data to approximate models, Advances in Heat Transfer 33 (1999) 295–414.

[2] F. Ogando, P. Velarde, Development of a radiation transport fluid dynamic code under AMR scheme, Journal of Quantitative Spectroscopy and Radiative Transfer 71 (2001) 541–550.

[3] R. Yang, G. Yuan, h-Refinement for simple corner balance scheme of S_N transport equation on distorted meshes, Journal of Quantitative Spectroscopy and Radiative Transfer 184 (2016) 241–253.

[4] M. Roger, C. Caliot, N. Crouseilles, P. Coelho, A hybrid transport-diffusion model for radiative transfer in absorbing and scattering media, Journal of Computational Physics 275 (2014) 346–362.

[5] P. J. Coelho, N. Crouseilles, P. Pereira, M. Roger, Multi-scale methods for the solution of the radiative transfer equation, Journal of Quantitative Spectroscopy and Radiative Transfer 172 (2016) 36–49.

[6] L. Soucasse, Ph. Rivière, A. Soufiani, Subgrid-scale model for radiative transfer in turbulent participating media, Journal of Computational Physics 257 (2014) 442–459.

[7] P. Benner, S. Gugercin, K. Willcox, A survey of projection-based model reduction methods for parametric dynamical systems, SIAM Review 57 (2015) 483–531.

[8] P. J. Schmid, Dynamic mode decomposition of numerical and experimental data, Journal of Fluid Mechanics (656) (2010) 5–28.

[9] F. Chinesta, A. Ammar, A. Leygue, R. Keunings, An overview of the proper generalized decomposition with applications in computational rheology, Journal of Non-Newtonian Fluid Mechanics 166 (2011) 578592.

[10] E. Videcoq, A. Neveu, O. Quemener, M. Girault, D. Petit, Comparison of two nonlinear model reduction techniques: The modal identification method and the branch eigenmodes reduction method, Numerical Heat Transfer, Part B: Fundamentals 49 (2006) 537–588.

[11] G. Berkooz, P. Holmes, J. L. Lumley, The proper orthogonal decomposition in the analysis of turbulent flows, Annual Review of Fluid Mechanics 25 (1993) 539–575.

[12] L. Sirovich, Turbulence and the dynamic of coherent structures. Part I: Coherent structures, Quarterly of Applied Mathematics 45 (3) (1987) 561–571.

[13] H. P. Bakewell, J. L. Lumley, Viscous sublayer and adjacent wall region in turbulent pipe flow, Physics of Fluids 10 (1967) 1880–1889.

[14] B. Podvin, P. Le Quéré, Low-order models for the flow in a differentially heated cavity, Physics of Fluids 13 (11) (2001) 3204–3214.

[15] F. Fang, T. Zhang, D. Pavlidis, C. Pain, A. Buchan, I. Navon, Reduced order modelling of an unstructured mesh air pollution model and application in 2d/3d urban street canyons, Atmospheric Environment 96 (2014) 96–106.

[16] R. Pinnau, A. Schulze, Model reduction techniques for frequency averaging in radiative heat transfer.

[17] A. G. Buchan, A. A. Calloo, M. G. Goffin, S. Dargaville, F. Fang, C. C. Pain, I. M. Navon, A POD reduced order model for resolving angular direction in neutron/photon transport problems, Journal of Computational Physics 296 (2015) 138157.

[18] J. Tencer, K. Carlberg, R. Hogan, M. Larsen, Reduced order modelling applied to the discrete ordinates method for radiation heat transfer in participating media, HT2016-7010, in: Proceedings of the 2016 Summer Heat Transfer Conference, ASME, Washington, DC, USA, 2016.

[19] J. Tencer, K. Carlberg, M. Larsen, R. Hogan, Accelerated solution of discrete ordinates approximation to the Boltzmann transport equation for a gray absorbing-emitting medium via model reduction, Journal of Heat Transfer 139 (2017) 122701.

[20] M. K. Denison, B. W. Webb, An absorption-line blackbody distribution function for efficient calculation of total gas radiative transfer, Journal of Quantitative Spectroscopy and Radiative Transfer 50 (5) (1993) 499–510.

[21] M. K. Denison, B. W. Webb, The spectral-line-based weighted-sum-of-gray-gases model in nonisothermal nonhomogeneous media, Journal of Heat Transfer 117 (1995) 359–365.

[22] L. Pierrot, Ph. Rivière, A. Soufiani, J. Taine, A fictitious-gas-based absorption distribution function global model for radiative transfer in hot gases, Journal of Quantitative Spectroscopy and Radiative Transfer 62 (1999) 609–624.

[23] M. F. Modest, H. Zhang, The full-spectrum correlated-k distribution for thermal radiation from molecular gas-particulate mixtures, Journal of Heat Transfer 124 (2002) 30–38.

[24] A. G. Buchan, A. S. Candy, S. R. Merton, C. C. Pain, J. I. Haidi, M. D. Eaton, A. J. H. Goddard, R. P. Smedley-Stevenson, The inner-element subgrid scale finite element method for the Boltzmann transport equation, Nuclear Science and Engineering 164 (2010) 105–121.

[25] A. G. Buchan, S. R. Merton, C. C. Pain, R. P. Smedley-Stevenson, Riemann boundary conditions for the Boltzmann transport equation using arbitrary angular approximations, Annals of Nuclear Energy 38 (2011) 1186–1195.

[26] S. Balay, S. Abhyankar, M. F. Adams, J. Brown, P. Brune, K. Buschelman, L. Dalcin, A. Dener, V. Eijkhout, W. D. Gropp, D. Kaushik, M. G. Knepley, D. A. May, L. C. McInnes, R. T. Mills, T. Munson, K. Rupp, P. Sanan, B. F. Smith, S. Zampini, H. Zhang, H. Zhang, PETSc users manual, Tech. Rep. ANL-95/11 - Revision 3.10, Argonne National Lab-

oratory (2018).
URL http://www.mcs.anl.gov/petsc

[27] L. Soucasse, Ph. Rivière, S. Xin, P. Le Quéré, A. Soufiani, Numerical study of coupled molecular gas radiation and natural convection in a differentially heated cubical cavity, Computational Thermal Sciences 4 (2012) 335–350.

[28] L. Soucasse, S. Dargaville, A. G. Buchan, C. C. Pain, A goal-based angular adaptivity method for thermal radiation modelling in non grey media, Journal of Quantitative Spectroscopy and Radiative Transfer 200 (2017) 215–224.

[29] A. G. Buchan, S. Dargaville, L. Soucasse, F. Fang, C. C. Pain, I. M. Navon, A reduced order model for optimally resolving the energy dependent angular direction for multi-group neutron particle transport, submitted to Journal of Computational Physics.

[30] C. C. Pain, A. P. Umpleby, C. R. E. de Oliveira, A. J. H. Goddard, Tetrahedral mesh optimisation and adaptivity for steady-state and transient finite element calculations, Computer Methods in Applied Mechanics and Engineering 190 (2001) 37713796.

[31] L. S. Rothman, I. E. Gordon, A. Barbe, D. Chris Benner, P. F. Bernath, M. Birk, V. Boudon, L. R. Brown, A. Campargue, J. P. Champion, K. Chance, L. H. Coudert, V. Dana, V. M. Devi, S. Fally, J. M. Flaud, R. R. Gamache, A. Goldman, D. Jacquemart, I. Kleiner, N. Lacome, W. J. Lafferty, J. Y. Mandin, S. T. Massie, S. N. Mikhailenko, C. E.

Miller, N. Moazzen-Ahmadi, O. V. Naumenko, A. V. Nikitin, J. Orphal, V. I. Perevalov, A. Perrin, A. Predoi-Cross, C. Rinsland, M. Rotger, M. Šimečková, M. A. H. Smith, K. Sung, S. A. Tashkun, J. Tennyson, R. A. Toth, A. C. Vandaele, J. Vander Auwera, The HITRAN 2008 molecular spectroscopic database, Journal of Quantitative Spectroscopy and Radiative Transfer 110 (2009) 533–572.

[32] R. Everson, L. Sirovich, KarhunenLoève procedure for gappy data, Journal of the Optical Society of America A 12 (8) (1995) 1657–1664.